

Intrinsic threshold electric field for domain wall motion in ferroelectrics based on discretized phase-field model

Huanhuan Tian and Jianguo Yang*
Zhangjiang Laboratory, Shanghai, China

Ming Liu†

Frontier Institute of Chip and System, Fudan University, Shanghai, China and
Institute of Microelectronics, Chinese Academy of Sciences, Beijing, China.

(Dated: September 20, 2024)

With the development of ferroelectric memories, it is becoming increasingly important to understand the ferroelectric switching behaviors at small applied electric fields. In this letter, we use a discretized phase-field model to systematically investigate the intrinsic threshold electric field (TEF) to drive flat 180° and 90° domain walls (DWs), and show that the results are qualitatively consistent with existing first-principles studies and experiments at cryogenic temperature. In addition, this work suggests that the activation electric field (AEF) observed in experiments at room temperature can be interpreted as the average of TEF behaviors of DWs with different curvatures, rather than explained by the traditional thermal nucleation theory. This work improves the understanding of DW motion kinetics at small applied fields, and shows that the mesh size and orientation are both important for the phase-field modeling of the above process.

In the last decade, ferroelectric memories have attracted extensive attention from the industry and academia [1–3], since the discovery of the new CMOS-compatible and scalable ferroelectric material, hafnia ferroelectrics, in 2011 [4]. Innovations to improve the performance of ferroelectric memories include coercive field reduction [5], non-destructive read [6], and high-density 3D architectures [6, 7], which all require in-depth understanding of ferroelectric switching especially at small applied electric fields.

Domain walls (DWs), which separate domains with different polarization directions but the same parent phase orientation, are commonly considered critical for ferroelectric switching [8]. Based on the symmetry of the parent phase, there exist 180°, 90°, 71°, and 109° DWs. The ferroelectric switching is generally believed to be controlled by two processes: the nucleation of reverse domains (the formation of DWs), and the DW motion [9, 10]. Electrical measurements cannot directly separate the two process, and can only provide an effective DW velocities v_{DW} , which is usually found to follow the Merz law [11, 12] at room temperature:

$$v_{DW} \sim \exp(-E_a/E_{app}), \quad (1)$$

where E_a is the activation electric field (AEF) for DW motion, and E_{app} is the applied electric field. Typically E_a is much larger than the coercive field E_c [13–15]. At cryogenic temperature, a sharp corner on v_{DW} - E curve has been observed in electrical measurements [16]:

$$v_{DW} \sim [\mathcal{R}(E_{app} - E_{th})]^\alpha, \quad (2)$$

where E_{th} is the threshold electric field (TEF) to drive DWs, $\mathcal{R}(\cdot)$ is the ramp function, and the index α is typically around 1. Apparently, E_{th} should be no larger than E_c [16, 17].

Different theories have been used to explain AEF and TEF for DW motion. Note that the continuum phase-field theory of a flat DW leads to E_{app} -independent DW mobility without AEF or TEF [18]. AEF has been widely explained by the thermally-activated nucleation of a triangle, square, or circular protrusion on existing flat 180° DWs [17, 19, 20]. However, this thermal nucleation theory predicts $E_a \sim 1/T$, leading to infinitely large E_a near cryogenic temperature, which contradicts the experimental observation. In addition, the assumption of protrusions on flat DWs seems to be artificial, which cannot be automatically reproduced in first-principles calculations and phase-field simulations. Indeed, first-principles calculations for ideally-flat DWs can also give an energy barrier for DW motion [17, 21–23], but in a TEF way. Such a barrier has been qualitatively explained by John W. Cahn using a discretized phase-field model [24]. Though very inspiring, Cahn’s work is limited to special cases (thick, flat 180° DW), has errors in derivations (discussed later in this work), and is underestimated in the community possibly due to the gap to explain the AEF observed in experiments.

In this letter, we systematically investigate the intrinsic TEF for flat and columnar DWs using a discretized phase-field model, and propose a new explanation for AEF without thermal nucleation. We study three types of DWs: one 180° DW, and two 90° DWs (“90 ↘↗” and “90 →↑”), as shown in Figure 1(a). We assume the numerical mesh coincides with unit cells in crystals. We then let the remnant dipole in each unit cell to be parallel to cell sides for 180° DW and “90 →↑” DW, but to cell diagonals for “90 ↘↗” DW. Note that the latter setting is not seen in real crystals and just to prove the

* yangjg@zjlab.ac.cn

† liuming@fudan.edu.cn

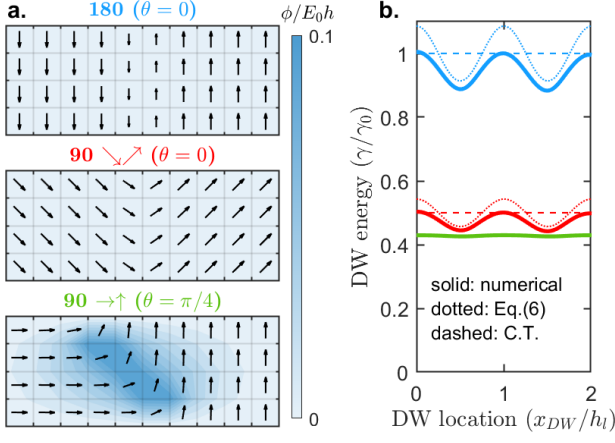


FIG. 1. (a) The equilibrium local polarization and electric potential, and (b) the DW motion barrier, for three types of DWs with $\delta/h_l = 0.8$ and $\eta/b = 3$. Electrodes (constant potentials) are placed on top and bottom boundaries. θ is to describe the DW orientation.

importance of mesh orientation.

We limit this work to the discussion of second-order phase transition of ferroelectrics, which can involve less parameters but more correlations, compared with first-order phase transition [25]. In addition, we ignore elastic energy, which is reasonable for stress-free boundary conditions and weak electrostriction. In this case, the total free energy for the ferroelectrics is [26]:

$$F = \int (f_{landau} + f_{grad} + f_{elec})dV, \quad (3)$$

where the Landau energy $f_{landau} = \frac{1}{2}a(P_x^2 + P_y^2) + \frac{1}{4}b(P_x^4 + P_y^4) + \frac{1}{2}\eta P_x^2 P_y^2$, the gradient energy $f_{grad} = \frac{1}{2}\kappa(|\nabla P_x|^2 + |\nabla P_y|^2)$, and the electrostatic energy $f_{elec} = -\mathbf{P} \cdot \mathbf{E} - \frac{1}{2}\epsilon_0 \epsilon_{r,b} |\mathbf{E}|^2$. Here P_x and P_y are polarization in x and y direction ($\mathbf{P} = [P_x, P_y]$), $\mathbf{E} = -\nabla\phi$ is the electric field, ϵ_0 is the vacuum permittivity, $\epsilon_{r,b}$ is the background relative permittivity, a, b, η are Landau parameters, and κ is the gradient penalty parameter. Then the dynamics of ferroelectric switching can be described by [26]

$$\frac{\tau}{\epsilon_0} \frac{\partial \mathbf{P}}{\partial t} = -\frac{\delta F}{\delta \mathbf{P}} \quad \text{and} \quad \nabla \cdot (\mathbf{P} + \epsilon_0 \epsilon_{r,b} \mathbf{E}) = 0 \quad (4)$$

in combination with proper boundary conditions, where τ is a time constant. We define the thickness of ferroelectric film as h . We assume that the energy minimum occurs at $[0, \pm P_0]$, $[\pm P_0, 0]$ for f_{landau} , and take into account other grain orientations by coordinate transformations. In addition, we assume E_{app} is positive if the applied field is pointing downward y axis.

We can derive the following intrinsic relations based on continuum theory. Note that $\eta \neq 3b$ leads to anisotropic permittivity, charged DWs, and absence of analytical solutions, for 90° switching [27]. Besides, continuum theory

predicts the same dynamics for “ $90 \rightarrow \uparrow$ ” and “ $90 \searrow \nearrow$ ” DW at the same E_{\parallel} (projection of applied field to the DW). (1) Basic properties: the remnant polarization $P_0 = \sqrt{-b/a}$, the longitudinal dielectric constant (parallel to \mathbf{P}) $\epsilon_{r,\parallel} = \epsilon_{r,b} + \frac{1}{\epsilon_0(a+3bP_0^2)}$ and the transverse dielectric constant (perpendicular to \mathbf{P}) $\epsilon_{r,\perp} = \epsilon_{r,b} + \frac{1}{\epsilon_0(a+\eta P_0^2)}$. (2) Bulk switching properties ($\eta = 3b$): the energy barrier $g_0 = \frac{1}{4}bP_0^4$ and TEF $E_0 = \frac{2}{3}\sqrt{\frac{1}{3}b}P_0^3$ for uniform 180° switching, the energy barrier $g_0/2$ and TEF $\frac{1}{\sqrt{2}}E_0$ for uniform 90° switching. (3) DW properties ($\eta = 3b$): the DW characteristic width $\delta = \frac{1}{P_0}\sqrt{\frac{2\kappa}{b}} = \frac{3\gamma_0}{8g_0}$ (around half real DW width), the energy $\gamma_0 = \frac{P_0^3}{3}\sqrt{8\kappa b}$ and mobility (DW normal velocity v_{DW} divided by E_{\parallel}) $\mu_0 = \frac{3\epsilon_0\delta}{2\tau P_0}$ for 180° DW [8, 28], and the energy $\gamma_0/2$ and mobility $\sqrt{2}\mu_0$ for 90° DW.

In the following, we turn to the discretized model. We apply finite volume method with staggered mesh for ϕ and \mathbf{P} , and assume equal size of mesh and unit cell as h_l . Figure 1 shows typical numerical solutions of the discretized model for the three DWs (given $\delta/h_l = 0.8$, $\eta = 3b$, $\epsilon_{r,b} = \epsilon_r/6$). As shown in Figure 1(a), the polarization is reduced near DWs, which should make switching easier compared with that in bulk domains. In addition, the “ $90 \rightarrow \uparrow$ ” DW perturbs the electric field while the 180° DW and the “ $90 \searrow \nearrow$ ” DW do not. The reason is that the bound charge of adjacent cells cannot be fully compensated in “ $90 \rightarrow \uparrow$ ” DW. Figure 1(b) shows the energy landscape for DW motion, extracted from the time evolution of total energy as DW proceeds at some applied field E_{app} (driven force has been subtracted). As expected, the total energy along with DW location has a period of h_l , due to translational symmetry, as also seen in first-principles studies [21, 22]. Since we put each dipole at the center of each cell, the energy peaks and valleys occur when DW passes the cell centers and edges, respectively. As a contrast, the continuum theory (C.T.) gives zero energy barrier since the total energy does not change with DW location. Furthermore, Figure 1(b) shows that the 180° DW has the highest DW motion barrier, followed by the “ $90 \searrow \nearrow$ ” DW, and then the “ $90 \rightarrow \uparrow$ ” DW.

Cahn was the first to seek to analytically derive the periodic picture of $\gamma(x_{DW})$ for 180° DW without nucleation theory [24]. He substituted the continuum solution $P = -P_0 + 2P_0 \tanh(\frac{x-x_{DW}}{\delta})$ into a discretized form of total energy $F = \sum_n \frac{1}{4}b(P_0^4 - P_n^4)$ [29] (where n is cell label) and then used Poisson summation to obtain:

$$\gamma_{180,ana1} = \gamma_0 \left[1 + 2\pi^2 \tilde{\delta} \left(1 - \frac{\pi^2 \tilde{\delta}^2}{2} \right) \text{csch}(\pi^2 \tilde{\delta}) \cos(2\pi \tilde{x}_{DW}) \right], \quad (5)$$

where $\tilde{\delta} = \delta/h_l$, $\tilde{x}_{DW} = x_{DW}/h_l$, and higher-order Fourier series have been neglected (valid if $\pi^2 \tilde{\delta} \gg 1$). This solution is actually unphysical, since the energy peaks occur when DW is at cell edges if $\tilde{\delta} \gg 1$ (but

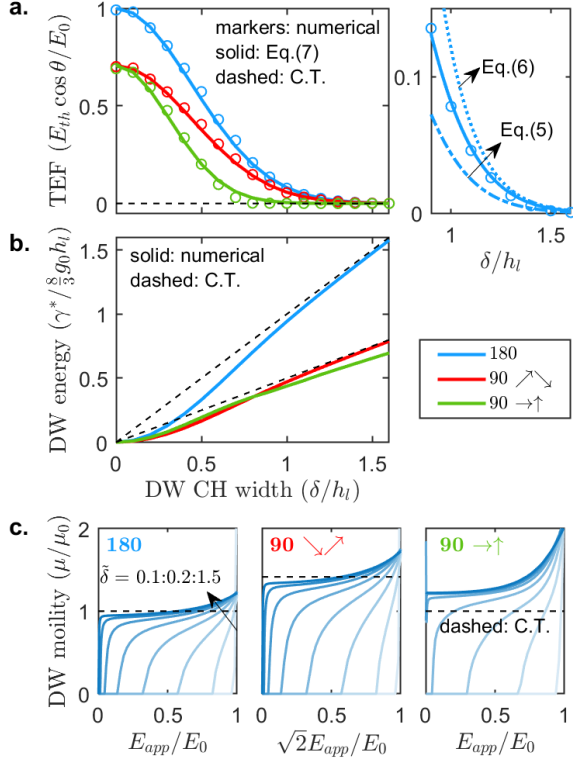


FIG. 2. (a) The threshold electric field (TEF), (b) DW energy, and (c) DW mobility for different DW characteristic (CH) length, based on the discretized model with $h = 8h_l$.

at cell centers if $\tilde{\delta} \ll 1$). To correct this mismatch, we derive another discretized form of total energy $F = \sum_n \frac{1}{2} b (P_0^2 - P_n^2)^2$ [30], and then arrive at a new expression of $\gamma(x_{DW})$:

$$\gamma_{180,ana2} = \gamma_0 [1 + 2\pi^2 \tilde{\delta} (1 + \pi^2 \tilde{\delta}^2) \text{csch}(\pi^2 \tilde{\delta}) \cos(2\pi \tilde{x}_{DW})], \quad (6)$$

which gives correct locations of extremums. Similarly, for “90° ↘↗” DW with $\eta = 3b$, we get $\gamma_{90, \searrow \nearrow, ana} = \frac{1}{2} \gamma_{180, ana}$ for both analytical solutions.

The comparison between $\gamma_{180,ana2}$, $\gamma_{90, \searrow \nearrow, ana2}$ and the numerical solution is shown in Figure 1(b). We can see that our analytical solution gives qualitatively correct pictures, though error still exists (even if we add more Fourier series) since the analytical solution has used the continuum solution of P in the derivation.

Once we get $\gamma(x_{DW})$, we can estimate the TEF (E_{th}) using $E_{th,ana} = \frac{1}{\cos \theta \Delta P} \left| \frac{\partial \gamma}{\partial x_{DW}} \right|_{max}$ ($\Delta P = 2P_0, \sqrt{2}P_0, \sqrt{2}P_0$ and $\theta = 0, 0, \pi/4$ for 180°, “90° ↘↗”, “90° →↑” DW, respectively). The results indicate that $E_{th,ana}$ decays to zero as $\tilde{\delta}$ goes to infinity, and $E_{th,90 \searrow \nearrow, ana} = \frac{1}{\sqrt{2}} E_{th,180,ana}$ if $\eta = 3b$, which trends are consistent with the numerical solution of E_{th} , as shown in Figure 2(a). However, Equation 5 underestimates TEF while Equation 6 overestimates TEF. In addition, the numerical solution also shows that E_{th} for DW

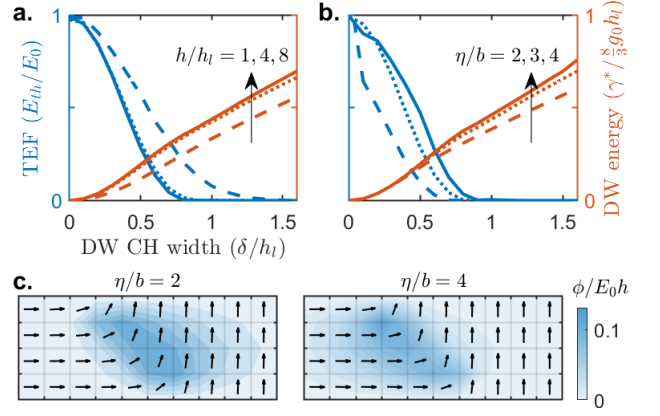


FIG. 3. The effect of (a) film thickness and (b) anisotropic factor η/b on the threshold electric field (TEF) and energy of “90° →↑” DW, and (c) the effect of η/b on local polarization and electric potential.

motion approaches that for uniform switching as δ goes to zero, which is not captured by Equation 5 or Equation 6. Therefore, we propose the following empirical model for the entire range of $\tilde{\delta}$:

$$E_{th,emp} = E_{th,uni} e^{-\alpha \tilde{\delta}^2}, \quad (7)$$

where $E_{th,uni} = E_0, \frac{1}{\sqrt{2}} E_0, E_0$, and $\alpha = \sqrt{2\pi}, \sqrt{2\pi}, 2\sqrt{2\pi}$ for 180°, “90° ↘↗”, “90° →↑” DW, respectively. This model fits numerical results quite well. “90° →↑” DW has smaller TEF than “90° ↘↗”, due to the distortion of electric field. Meanwhile, Figure 2(b) shows that the stable DW energy ($\gamma^* = \min(\gamma)$) monotonically increases with $\tilde{\delta}$, and is overestimated by the continuum theory at small $\tilde{\delta}$. In addition, as shown in Figure 2(c), the mobility ($\mu \doteq v_{DW,x} / E_{app}$) of 180° and “90° ↘↗” DW goes to zero for small E_{app} and small $\tilde{\delta}$, and approaches the continuum theory for large E and large δ . “90° →↑” DW moves faster than that predicted by continuum theory even for thick DWs.

The trend of increasing E_{th} with decreasing γ^* and δ shown in Figure 2 for 180° DW and “90° →↑” DW is roughly consistent with the existing first-principles studies. For HfO_2 , it has been shown that the switching barrier of near-zero-energy flat-phonon-band 180° DW is close to that of uniform switching [22], and that of the high-energy quasi-chiral 180° DW ($\tilde{\delta} \in [0.5, 1]$) is small and comparable with experimental observation ($E_{th}/E_0 \sim 0.15$, stress-free condition) [21]. For PbTiO_3 , it has been show that 90° DW has a much smaller energy [31] and TEF [17] compared with 180° DWs. This indicates that a two-step sequential 90° DW motion may be energetically more favorable compared with one 180° DW motion. Note that the approach presented in this work can be extended to f_{landau} with more terms (which may give first-order transition) to better fit the first-principles results.

Next, we present the effect of film thickness h ,

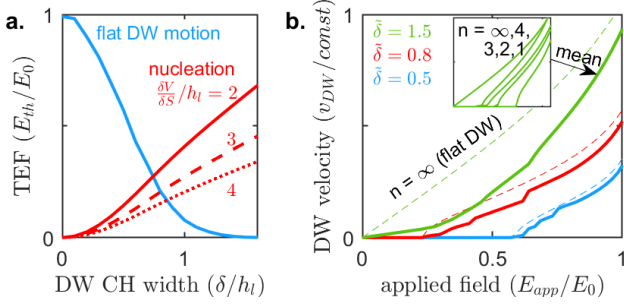


FIG. 4. (a) The threshold electric field (TEF) for motion of flat 180° DW based on the discretized model (blue), and the growth of existing nuclei based on continuum theory (red). (b) The averaged DW velocity versus applied electric field for a collection of columnar 180° DWs with different nucleus size.

anisotropic factor $\eta/3b$, and background permittivity $\epsilon_{r,b}$ for “ $90 \rightarrow \uparrow$ ” DW. These three parameters do not influence the 180° DW, and h does not influence “ $90 \searrow \uparrow$ ” DW. As already shown in Figure 1(a), the electric field is distorted near electrodes. Figure 3(a) shows that this distortion does not change TEF and DW energy much for films thicker than $4h_l$ (typically ~ 2 nm). Figure 3(b) shows that smaller η/b leads to smaller TEF and γ^* , which can be explained by the asymmetric electric field on the two sides of DWs as shown in Figure 3(c). Note that the above trend can be reversed for E_{app} in the other direction. The background permittivity has negligible effect on TEF and DW energy (not shown in Figure 3).

Finally, we turn to the motion of columnar DWs, which should be common in real ferroelectric thin films. The continuum theory (assuming $\delta \ll r_c$) leads to an additional TEF $\gamma^*/2P_0r_c$ to drive a columnar DW with characteristic curvature radius $r_c = \frac{\delta V}{\partial S}$ (r_c equals the radius for cylindrical DWs), where V and S are the domain volume and DW area, respectively. As shown in Figure 4(a), this curvature effect is stronger for thicker DWs. Then we directly simulate the 3D 180° DW motion (with \mathbf{P} in y direction and DW velocity in x and z direction) for a distance of $6h_l$ near existing nuclei (where P is fixed to $[0, -P_0]$) with size $n \times n$ ($n = 1, 2, 3, 4, \infty$ in the unit of h_l , and $n = \infty$ represents the flat DW). Such a wide size dis-

tribution of existing nuclei can exist in real films due to defects such as grain boundaries [32]. As shown in Figure 4(b), thin DWs are rarely influenced by the curvatures, and the averaged DW velocity holds the TEF behavior (Equation 2). For thick DWs, there is a large distribution of TEF for different curvatures, and the averaged DW velocity clearly shows AEF behavior (Equation 1).

Therefore, we propose that AEF observed in experiments at room temperature can be explained by the average behavior of TEF for thick DWs with different curvatures induced by defects such as grain boundaries. In terms of the transition of AEF to TEF at cryogenic temperature, we suggest two possible explanations: (1) the DW energy is higher at lower temperature, resulting in smaller and fewer nuclei near defects, which prevents switching at small fields; (2) the DWs are significantly thinner at lower temperature, and thus are less influenced by curvatures and show TEF behaviors. According to Landau theory of second-order phase transition, κ, b, η, τ does not change with temperature while $a = a_0(T - T_c)$ (where T_c is the Curie temperature), leading to $\gamma \sim |T - T_c|^{3/2}$ and $\delta \sim |T - T_c|^{-1/2}$ [25]. However, these laws have few experimental or first-principles validations. One x-ray diffraction study found that $\delta \sim |T - T_c|^{-1}$ for LaAlO_3 [33]. The exact description of the temperature dependence of DW energy and thickness is beyond the scope of this work and will be studied in the future.

In summary, we investigate the threshold electric field (TEF) for a wide range of DW width and energy for flat 180° and 90° DWs and columnar 180° DWs, based on a discretized 2nd-order transition phase-field model. We present numerical results, analytical approximations, and empirical model for the TEF of flat DWs, which is qualitatively consistent with existing first-principles studies. In addition, we show that the activation electric field (AEF) in Merz law can be explained by a collection of TEF of columnar DWs with different curvatures, without including thermal nucleation theory. Furthermore, our results also demonstrate that the mesh size and mesh orientation in phase-field simulations must be carefully treated when studying the low-field switching behaviours.

This work was supported in part by the NSFC under Grants 92164204, 62222119.

-
- [1] U. Schroeder, M. H. Park, T. Mikolajick, and C. S. Hwang, *Nat Rev Mater* **7**, 653 (2022).
 [2] N. Ramaswamy, A. Calderoni, J. Zahurak, G. Servalli, A. Chavan, S. Chhajer, M. Balakrishnan, M. Fischer, M. Hollander, D. P. Ettisserry, A. Liao, K. Karda, M. Jerry, M. Mariani, A. Visconti, B. R. Cook, B. D. Cook, D. Mills, A. Torsi, C. Mouli, E. Byers, M. Helm, S. Pawlowski, S. Shiratake, and N. Chandrasekaran, in *2023 International Electron Devices Meeting (IEDM)* (IEEE, San Francisco, CA, USA, 2023) pp. 1–4.
 [3] J. P. B. Silva, R. Alcalá, U. E. Avci, N. Barrett, L. Bégon-

- Lours, M. Borg, S. Byun, S.-C. Chang, S.-W. Cheong, D.-H. Choe, J. Coignus, V. Deshpande, A. Dimoulas, C. Dubourdieu, I. Fina, H. Funakubo, L. Grenouillet, A. Gruverman, J. Heo, M. Hoffmann, H. A. Hsain, F.-T. Huang, C. S. Hwang, J. Íñiguez, J. L. Jones, I. V. Karpov, A. Kersch, T. Kwon, S. Lancaster, M. Lederer, Y. Lee, P. D. Lomenzo, L. W. Martin, S. Martin, S. Migita, T. Mikolajick, B. Noheda, M. H. Park, K. M. Rabe, S. Salahuddin, F. Sánchez, K. Seidel, T. Shimizu, T. Shiraishi, S. Slesazek, A. Toriumi, H. Uchida, B. Vilquin, X. Xu, K. H. Ye, and U. Schroeder, *APL Materials* **11**,

- 089201 (2023).
- [4] T. S. Böske, J. Müller, D. Bräuhaus, U. Schröder, and U. Böttger, *Applied Physics Letters* **99**, 102903 (2011).
- [5] Y. Wang, L. Tao, R. Guzman, Q. Luo, W. Zhou, Y. Yang, Y. Wei, Y. Liu, P. Jiang, Y. Chen, S. Lv, Y. Ding, W. Wei, T. Gong, Y. Wang, Q. Liu, S. Du, and M. Liu, *Science* **381**, 558 (2023).
- [6] S. Deng, Y. Xiao, Z. Zhao, T.-J. Huang, T. Kampfe, V. Narayanan, and K. Ni, in *2023 International Electron Devices Meeting (IEDM)* (IEEE, San Francisco, CA, USA, 2023) pp. 1–4.
- [7] Z. Fu, S. Cao, H. Zheng, J. Luo, Q. Huang, and R. Huang, in *2023 International Electron Devices Meeting (IEDM)* (IEEE, San Francisco, CA, USA, 2023) pp. 1–4.
- [8] A. K. Tagantsev, L. E. Cross, and J. Fousek, *Domains in Ferroic Crystals and Thin Films* (Springer New York, New York, NY, 2010).
- [9] Y. Ishibashi and Y. Takagi, *J. Phys. Soc. Jpn.* **31**, 506 (1971).
- [10] A. K. Tagantsev, I. Stolichnov, N. Setter, J. S. Cross, and M. Tsukada, *Phys. Rev. B* **66**, 214109 (2002).
- [11] W. J. Merz, *Journal of Applied Physics* **27**, 938 (1956).
- [12] C. F. Pulvari and W. Kuebler, *Journal of Applied Physics* **29**, 1315 (1958).
- [13] W. J. Merz, *Phys. Rev.* **95**, 690 (1954).
- [14] D. H. Lee, Y. Lee, K. Yang, J. Y. Park, S. H. Kim, P. R. S. Reddy, M. Materano, H. Mulaosmanovic, T. Mikolajick, J. L. Jones, U. Schroeder, and M. H. Park, *Applied Physics Reviews* **8**, 021312 (2021).
- [15] C. Alessandri, P. Pandey, A. Abusleme, and A. Seabaugh, *IEEE Electron Device Lett.* **39**, 1780 (2018).
- [16] J. Y. Jo, S. M. Yang, T. H. Kim, H. N. Lee, J.-G. Yoon, S. Park, Y. Jo, M. H. Jung, and T. W. Noh, *Phys. Rev. Lett.* **102**, 045701 (2009).
- [17] S. Liu, I. Grinberg, and A. M. Rappe, *Nature* **534**, 360 (2016), publisher: Nature Publishing Group.
- [18] Y. Su and C. M. Landis, *Journal of the Mechanics and Physics of Solids* **55**, 280 (2007).
- [19] R. C. Miller and G. Weinreich, *Physical Review* **117**, 1460 (1960).
- [20] Y.-H. Shin, I. Grinberg, I.-W. Chen, and A. M. Rappe, *Nature* **449**, 881 (2007).
- [21] D.-H. Choe, S. Kim, T. Moon, S. Jo, H. Bae, S.-G. Nam, Y. S. Lee, and J. Heo, *Materials Today* **50**, 8 (2021).
- [22] H.-J. Lee, M. Lee, K. Lee, J. Jo, H. Yang, Y. Kim, S. C. Chae, U. Waghmare, and J. H. Lee, *Science* **369**, 1343 (2020).
- [23] W. Ding, Y. Zhang, L. Tao, Q. Yang, and Y. Zhou, *Acta Materialia* **196**, 556 (2020).
- [24] J. W. Cahn, *Acta Metallurgica* **8**, 554 (1960).
- [25] P. Chandra and P. B. Littlewood, in *Physics of Ferroelectrics*, Vol. 105 (Springer Berlin Heidelberg, Berlin, Heidelberg, 2007) pp. 69–116, series Title: Topics in Applied Physics.
- [26] J.-J. Wang, B. Wang, and L.-Q. Chen, *Annu. Rev. Mater. Res.* **49**, 127 (2019).
- [27] Y. Xiao, V. B. Shenoy, and K. Bhattacharya, *Phys. Rev. Lett.* **95**, 247603 (2005).
- [28] M. A. Collins, A. Blumen, J. F. Currie, and J. Ross, *Phys. Rev. B* **19**, 3630 (1979).
- [29] The key step of this derivation is $\sum_n f_{grad,n} = \frac{\kappa}{2\hbar_l^2} \sum_n (P_{n+1} - P_n)^2 = \frac{\kappa}{2\hbar_l^2} \sum_n P_n (2P_n - P_{n-1} - P_{n+1}) = \frac{1}{2} \sum_n P_n \left(\frac{\partial f_{Landau}}{\partial P} \right)_n$.
- [30] The key step of this derivation is to use $P_n - P_{n-1} \approx P_0 \left(1 - \left(\frac{P_n}{P_0} \right)^2 \right) \frac{\hbar_l}{\delta}$ (using the Taylor expansion of the tanh function) to calculate the gradient energy $\frac{\kappa}{2\hbar_l^2} \sum_n (P_{n+1} - P_n)^2$.
- [31] B. Meyer and D. Vanderbilt, *Phys. Rev. B* **65**, 104111 (2002).
- [32] S. Choudhury, Y. Li, C. Krill Iii, and L. Chen, *Acta Materialia* **55**, 1415 (2007).
- [33] J. Chrosch and E. K. H. Salje, *Journal of Applied Physics* **85**, 722 (1999).